Title: Computational model for synthesizing auditory brainstem responses to assess neuronal alterations in aging and autistic animal models

Abbreviated title: Model for simulating auditory brainstem response

Ben-Zheng Li*[1], Shani Poleg*[1], Matthew Ridenour[1], Daniel Tollin[1], Tim Lei[2], and Achim Klug[1]

* indicates equal contribution

1 = Department of Physiology & Biophysics, University of Colorado School of Medicine, Aurora, Colorado, USA

2 = Department of Electrical Engineering, University of Colorado, Denver, Denver, CO, United States

All correspondence should be addressed to:

Achim Klug, PhD, Department of Physiology & Biophysics

RC2: Rm 9120, MS 8625, 12700 E. 19th Avenue, University of Colorado School of Medicine

Aurora, CO 80045, USA. E-mails: achim.klug@CUAnschutz.edu, Phone: 303-724-4621.

Financial interests or conflicts of interest (if applicable): none

Acknowledgements:

This work was funded by NIH-NIDCD R01 DC017924 (MPIs: Tollin and Klug). This work utilized the Alpine High Performance Computing Resource at the University of Colorado Boulder. Alpine is jointly funded by the University of Colorado Boulder, the University of Colorado Anschutz, Colorado State University, and the National Science Foundation (award 2201538).

Abstract:

The auditory brainstem response (ABR) is a widely used objective electrophysiology measure for non-invasively assessing auditory function and neural activities in the auditory brainstem, but its ability to reflect detailed neuronal processes is limited due to the averaging nature of the electroencephalogram recordings. This study addresses this limitation by developing a computational model of the auditory brainstem which is capable of synthesizing ABR traces based on a large, population scale neural extrapolation of a spiking neuronal network of auditory brainstem neural circuitry. The model was able to recapitulate alterations in ABR waveform morphology that have been shown to be present in two medical conditions: animal models of autism and aging. Moreover, in both of these conditions, these ABR alterations are caused by known distinct changes in auditory brainstem physiology, and the model could recapitulate these changes. In the autism model, the simulation revealed myelin deficits and hyperexcitability, which caused a decreased wave III amplitude and a prolonged wave III-V interval, consistent with experimentally recorded ABRs in Fmr1-KO mice. In the aging model, the model recapitulated ABRs recorded in aged gerbils and indicated a reduction in activity in the medial nucleus of the trapezoid body (MNTB), a finding validated by confocal imaging data. These results demonstrate not only the model's accuracy but also its capability of linking features of ABR morphologies to underlying neuronal properties and suggesting follow-up physiological experiments.

Significance Statement (120 words maximum):

This study presents a novel computational model of the auditory brainstem, capable of synthesizing auditory brainstem response (ABR) traces by simulating large-scale neuronal activities. Addressing limitations of traditional ABR measurements, the model links ABR waveform features to underlying neuronal properties. Validated using empirical ABRs from animal models of autism and aging, the model accurately reproduced observed ABR alterations, revealing influences of myelin deficits and hyperexcitability in Fragile X syndrome, and degraded inhibitory activity in aging. These findings, supported by experimental data, demonstrate the model's potential for predicting changes in auditory brainstem physiology and guiding further physiological investigations, thus advancing our understanding of auditory neural processes.

Introduction:

The auditory brainstem response (ABR) is a non-invasive or minimally invasive electrophysiological measurement of auditory evoked potentials created by auditory brainstem nuclei. To record ABRs, small, brief and in our case multifrequency sound stimuli (clicks) were presented to rodents. These clicks recruited simultaneous action potentials in auditory nerve fibers which can be measured noninvasively through the skull as wave I. As this activity ascends the lower auditory system, subsequent waves II to V are created, representing neural activity along the ascending auditory pathway (Møller and Jannetta, 1985). This technique allows for simultaneous objective assessment of multiple stages of the auditory system, making it a useful tool for non-invasively detecting hearing impairments in clinical settings (Johnson et al., 2005) as well as a frequently used tool in hearing research studies to investigate auditory dysfunction and underlying neurological disorders (Santos et al., 2017).

However, the ABR only measures the overall neural activity at each stage due to the use of low impedance electrodes which are placed outside the skull, similar in nature to EEG recordings which average across all neurons. Some stages, quantified as one single wave, may contain neural circuits with multiple nuclei and steps of auditory information processing, such as signal sharpening, coincidence detection, and sound localization (Grothe et al., 2010; Oertel et al., 2017). These simultaneous activity patterns may not be independently reflected in ABR wave metrics and typically necessitate alternative methods of measurements such as patch-clamp, extracellular recordings or optogenetic manipulation (Hernandez et al., 2014; Beiderbeck et al., 2018; Keplinger et al., 2018). Similarly, computational models for auditory information processing typically use parameters and measurements from single cell data (e.g., Ashida et al., 2016; Li et al., 2022). Validating model predictions involving the propagation and transformation of auditory information across multiple stations of the ascending auditory system may require recordings and interventions at multiple stages in a large population size, which is experimentally challenging and difficult to achieve at cellular level resolution.

Therefore, there is a need to predict ABR waveforms from underlying cellular properties as well as a need to be able to predict changes in cellular physiology from alterations in global ABR morphologies. Several sophisticated ABR models are available to date. However, they are either based on population-level firing rates (Melcher and Kiang, 1996; Verhulst et al., 2015, 2018), lacking the ability to address detailed biophysical properties and membrane dynamics for single neurons, or they are based on simulating only a single stage of the auditory brainstem (Rattay and Danner, 2014; Saiz-Alía and Reichenbach, 2020). Hence, there is a need for a computational model that involves the entire ascending neural circuitry of the auditory brainstem and simulates the complete ABR trace.

In this study, we developed a computational model of the auditory brainstem that can perform large-scale neural simulations of the afferent auditory pathway and synthesize ABRs I through V based on simulated neuronal activities evoked by modeled sound wave stimulation. We validated this model by computing the ABR of an autistic (Fragile X) animal line based on previously reported alterations and myelin deficits in Fragile X. We observed morphologically altered ABRs with decreased wave III and prolonged wave III-V, which were then validated with experimentally recorded ABRs from *Fmr1*-KO mice versus wild-type controls. Furthermore, this model was also used to predict alterations in the ABR recorded from aging gerbils, revealing a decreased population size in the medial nucleus of the trapezoid body (MNTB). This latter finding was experimentally verified by counting the number of MNTB cells in confocal image datasets captured from brain sections of aging gerbils.

Materials and Methods:

ABR acquisition

The ABR recording procedures are similar to the approaches described in previous publications (Benichoux et al., 2018; McCullagh et al., 2020; Poleg et al., 2024) and illustrated in Fig.1. ABRs were measured from *Fmr1*-KO mice (N = 22, 13 males and 9 females) and C57BL/6 wildtype mice (N = 20, 12 males and 8 females) with an age range of 73.03 ± 11.64 (Mean ± SD) days old. Animals were anaesthetized with a mixture of ketamine and xylazine by intraperitoneal injections. Platinum needle electrodes were placed under the skin at the apex (recording site), nape (reference), and back leg (ground) after the toe-pinch reflex disappeared. Sound stimuli were 0.2-ms complex clicks with 35 ± 5 ms (Mean ± SD) interstimulus intervals and were delivered by a pair of speakers (MF-1 multi-field speakers, Tucker Davis Technologies, Alachua, FL, USA) which received amplified soundwaves generated by a customized Python script. Recorded traces were filtered using a 50-3000 Hz second-order bandpass filter and averaged across 1000 repetitions per condition, i.e., binaural, left monaural, and right monaural. In addition, the binaural hearing and spatial hearing were also assessed by the binaural interaction component (BIC) of the ABR. The BIC was calculated by calculating the difference between the sum of the two (left and right ear) monaural ABRs minus the ABR recorded with binaural sound stimulation on a point-by-point basis (Laumen et al., 2016a; Benichoux et al., 2018). All experimental procedures were reviewed and approved by the institutional animal care and use committees (IACUC) of the University of Colorado Anschutz Medical Campus (permit no.00617) and complied with all National Institutes of Health (NIH) and OLAW guidelines for the humane treatment of laboratory animals.

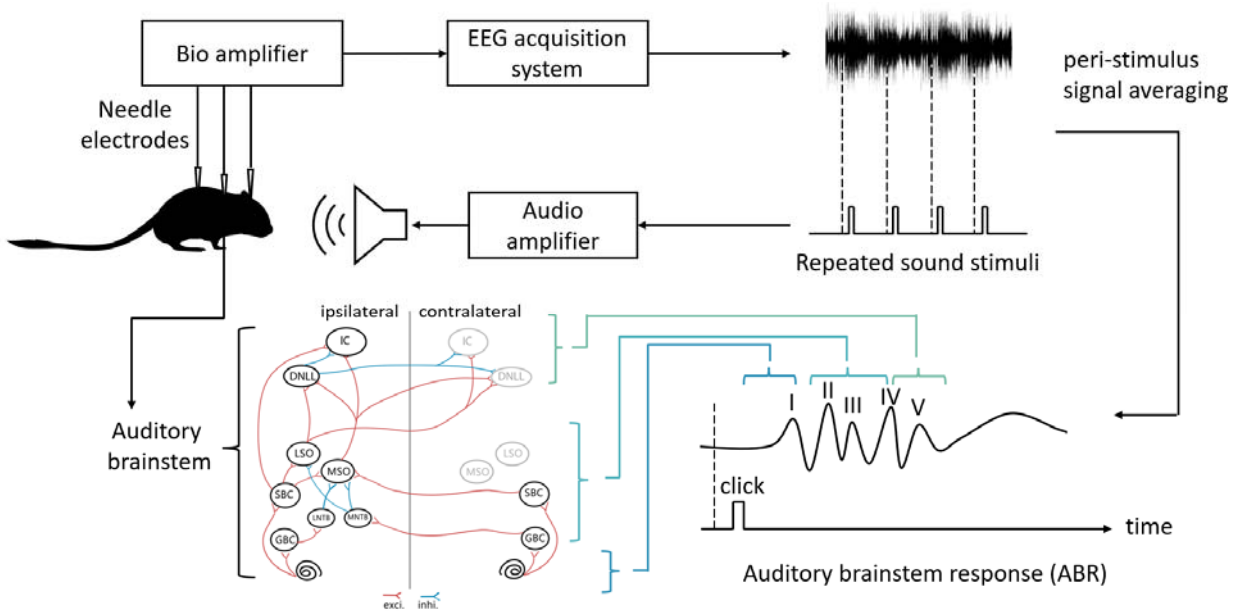

Figure 1. Schematic of the ABR recording setup (top) and sources of ABR waves (bottom).

Neuron and synapse models

Spiking neurons are the most basic building block to construct the expected auditory brainstem model. Multiple spiking neuron models are available, ranging from the leaky integrate-and-fire model, the Izhikevich model (Izhikevich, 2003), up to much more biophysically realistic (and computationally demanding) the Hodgkin-Huxley (Hodgkin and Huxley, 1952) and multicompartment models. Among these options, the most computationally efficient one is the conductance-based leaky integrate-and-fire model. The dynamic of the membrane potential is described by the following equation:

, where is the membrane potential, is the membrane capacitance, is the synaptic current, is the leak current, is the leaky conductance, is the leaky reversal potential, and is the membrane time constant. The leaky integrate-and-fire neuron emits a spike when its membrane potential reaches the firing threshold , and the membrane potential resets to subsequently.

Synapses can be either simulated by a conductance-based model or a current-based model. In the conductance-based model, the synaptic current is given by the product of the conductance and the driving force,

$$I_{syn} = g_e(E_e - v_m) + g_i(E_i - v_m)$$

$$\tau_e \frac{dg_e}{dt} = -g_e$$

$$\tau_i \frac{dg_i}{dt} = -g_i$$

, where g_e is the excitatory conductance, g_i is the inhibitory conductance, E_e is the reversal potential of excitatory synapses, E_i is the reversal potential of inhibitory synapses, and τ_e and τ_i are corresponding time constant. For each incoming spike, the presynaptic membrane induces an increment of postsynaptic conductance (Δg_e or Δg_i, dependent on the synapse type).

The reported simulation results were modeled with a conductance-based leaky integrate and fire model with all parameters used listed in the Tab.1.

Table 1. List of parameters for neurons and synapses

Neuron parameter	**Value**	**Description**	**Synapse Parameter**	**Value**	**Description**
C_m	70 pF	membrane capacitance	E_e	0 mV	excitatory reversal potential
V_{th}	-50 mV	threshold potential	E_i	-70 mV	inhibitory reversal potential

V_{reset}	-55.8 mV	reset potential	Δg_{exci}	15 nS [a]	excitatory postsynaptic conductance increment
τ_{ref}	5 ms	refractory period	Δg_{inhi}	10 nS [b]	inhibitory postsynaptic conductance increment
E_l	-55.9 mV	leaky reversal potential	τ_e	0.23 ms	excitatory time constant
g_l	13 nS	leaky conductance	τ_i	2 ms	Inhibitory time constant

a. Δg_{exci} = 100 nS for the calyx of Held in the GBC-to-MNTB projection

b. Δg_{inhi} = 75 nS for the inhibitory projections to the MSO

Network model

The network architecture (Fig.2) of the auditory brainstem model reported here is based on our previous spiking network model of the medial superior olive (MSO) circuit (Li et al., 2022) extended to simulate the major components of the auditory afferent pathway and auditory nuclei that facilitate ABRs. The Brian2 simulator (Stimberg et al., 2019) was used for the implementation of this network model. The computation was performed on the supercomputing cluster at the University of Colorado Boulder (Alpine High Performance Computing Cluster).

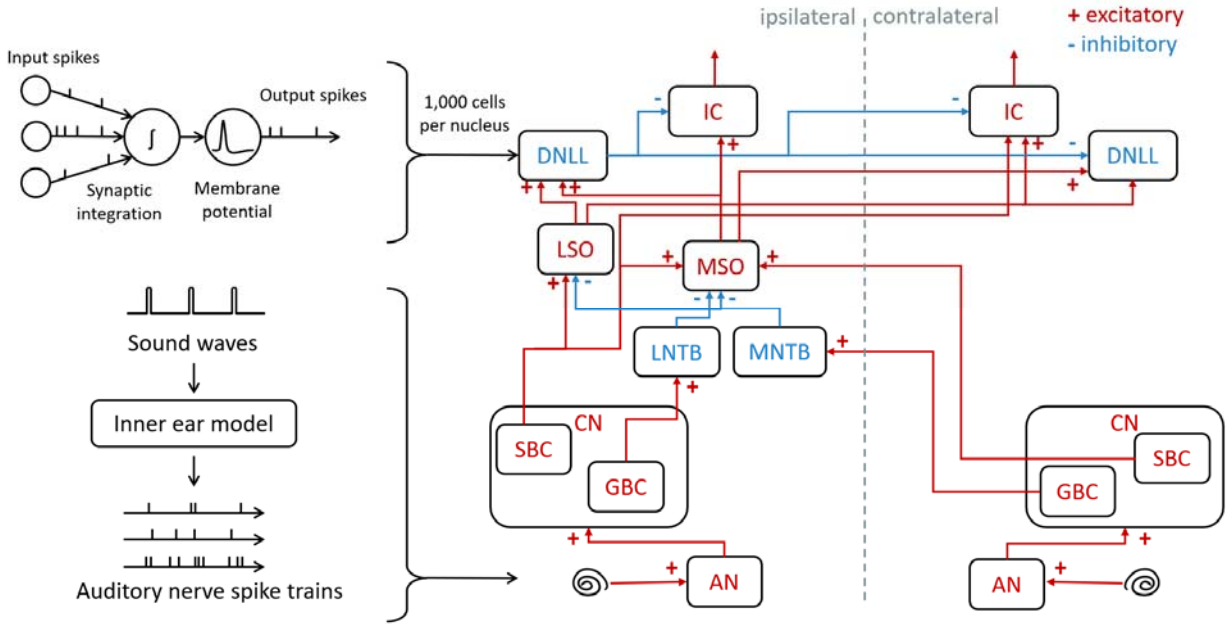

Figure 2. Network architecture of the auditory brainstem model.

In this model, sound waves are encoded into cochlear responses using Zilany's model (Zilany et al., 2014), implemented in the cochlear package (Rudnicki et al., 2015), which allows for the encoding of arbitrary sound waves such as pure tones, modulated tones, chirps and natural sounds. A 100-μs complex click sound with 100 ms inter-stimulus interval was utilized for simulating click ABRs. To simulate the auditory nerve activity, we used 60% high spontaneous firing fibers, 20% medium spontaneous firing fibers and 20% low spontaneous firing fibers (e.g., Liberman, 1978). According to the neural circuit architecture of auditory brainstem (Grothe et al., 2010), cochlear responses encoded from the auditory stimuli are sent to the brain through the auditory nerve (AN) and are received at the cochlear nuclei (CN). In the CN, the spherical bushy cells (SBCs) innervate medial superior olive (MSO) neurons bilaterally, lateral superior olive (LSO) neurons ipsilaterally, and inferior colliculus (IC) neurons contralaterally. Globular bushy cells (GBCs) innervate the contralateral medial nucleus of the trapezoid body (MNTB) and the ipsilateral lateral nucleus of the trapezoid body (LNTB). The MSO receives bilateral excitation from SBCs, contralateral inhibition via MNTB, and ipsilateral inhibition via LNTB. Meanwhile, the LSO receives ipsilateral excitation from SBC and contralateral inhibition via MNTB. Next, MSO innervates IC

ipsilaterally and dorsal nuclei of lateral lemniscus (DNLL) bilaterally, and LSO innervates the ipsilateral DNLL and the contralateral IC. Finally, DNLL inhibits bilateral ICs and contralateral DNLL.

In this model, every neural population contained one thousand spiking neurons that stochastically connected to neurons in corresponding populations with a connection probability ($p_{connect}$), an axonal transmission delay (t_{trans}), and a synaptic delay (t_{syn}). The detailed parameters of the connectivity were adopted from previous studies (Brand et al., 2002; Spirou et al., 2005; Couchman et al., 2010; Roberts et al., 2014; Encke and Hemmert, 2018; Li et al., 2022) and are listed in Table 2. The delays in the network were randomly assigned to each synaptic connection using the mean value listed in Tab.2 with a standard deviation of 50 microseconds. The t_{trans} of synaptic connections from contralateral side were estimated by the fiber myelin thickness and varied in the result section.

Table 2. List of network parameters for the auditory brainstem model

Population	**Type**	**Connection**	$\boldsymbol{p_{connect}}$	$\bar{\boldsymbol{t}}_{trans}$ **(ms)**	$\bar{\boldsymbol{t}}_{syn}$ **(ms)**
AN	Spike generator	AN → ipsi. GBC	4 %	0.2	0.6
		AN → ipsi. SBC	4 %	0.2	0.6
SBC	Excitatory	SBC → ipsi. MSO	0.6 %	0.6	0.6
		SBC → cont. MSO	0.6 %	0.8	0.6
		SBC → ipsi. LSO	4 %	0.6	0.6
		SBC → cont. IC	0.4 %	0.8	0.6
GBC	Excitatory	GBC→ ipsi. LNTB	0.3 %	0.3	0.3
		GBC→ cont. MNTB	one-to-one	0.4	0.2
MNTB	Inhibitory	MNTB → ipsi. MSO	0.3 %	0.1	0.3

		MNTB → ipsi. LSO	0.8 %	0.1	0.3
LNTB	Inhibitory	LNTB → ipsi. MSO	0.3 %	0.1	0.3
MSO	Excitatory	MSO → DNLL MSO → ipsi. IC	0.4 % 0.8 %	0.3 0.3	0.3 0.3
LSO	Excitatory	LSO → DNLL LSO → contra. IC	0.4 % 0.8 %	0.3 0.3	0.3 0.3
DNLL	Inhibitory	DNLL → contra. DNLL DNLL → IC	0.4 % 0.2 %	0.3 0.3	0.3 0.3
IC	Excitatory				

Simulated ABRs

The population responses of each modeled nucleus (Fig.3a), driven by the click sound activity, were calculated separately as the peri-stimulus time histograms shown in Fig.3b. The field potentials for each nucleus were approximated using instantaneous firing rates calculated using a Gaussian filter with a kernel standard deviation of 0.05 ms on the population of spike trains from each stimulation (Fig.3c) (Melcher and Kiang, 1996; Verhulst et al., 2018). These field potentials were then assumed to have originated at specific spatial locations based on the geometric arrangement of these nuclei in the brain atlas for the desired species such as gerbil (Radtke-Schuller et al., 2016), mouse (Chon et al., 2019), or human (Fan et al., 2016). With the location of the electrode overlayed, the Euclidean distances between nucleus centers and electrodes were calculated, and the field potentials propagated from the nuclei were estimated with amplitudes exponentially attenuating with distance, as well as the propagation latency linearly increasing with distance, assuming 50 m/s (Fig.3d). The single-trial ABR traces were then generated through integrating the field potentials of all simulated nuclei at the recording location, and the raw ABR trace was obtained by taking peri-stimulus signals averaged across all single-trial traces (Fig.3e).

Finally, a detrend filter was applied to obtain clearer peak amplitudes and latencies, and to produce higher compatibility with existing ABR recordings from experiments.

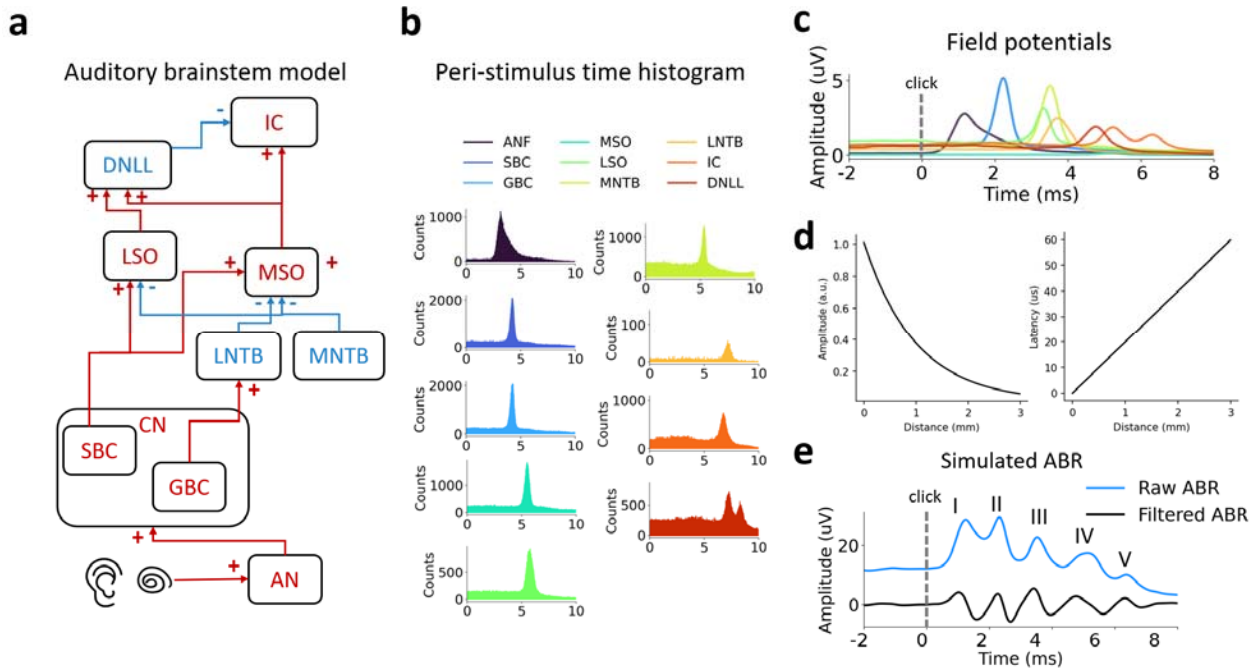

Figure 3. Workflow of modeling ABRs. (a) The auditory brain stem that was modeled. (b) Peri-stimulus time histograms induced by encoding click sounds averaged across all neurons for each nucleus. (c) Approximated field potentials from histograms. (d) Exponentially attenuated amplitudes and linearly increased latencies for field potentials propagating over distance. (e) Final ABRs modeled by propagating and integrating field potentials according to the geometric distribution of the nuclei and electrode location.

ABR analysis

Experimentally recorded ABRs were analyzed with the same workflow. The raw traces were first filtered with a Butterworth bandpass filter (100-3000 Hz, 2nd order), and detrended by a Savitzky-Golay filter. Then, ABR waves were detected by searching for local maxima, and labeled sequentially. Manual inspections were performed, and adjustments made when misclassification occurred. The ABR peak thresholds were defined as 10 dB SPL below the minimum sound level with visually detectable peaks. The cross-correlation (xCorr) ABR thresholds were automatically computed based on curves fitted with

sigmoids of the cross-correlations between adjacent sound levels (Suthakar and Liberman, 2019). The peak amplitude, area, latency and inter-peak intervals were measured as the peak metrics for characterizing ABR waves and BIC DN1. Statistical differences in the peak metrics were tested by using the two-sided Mann-Whiteney U test at sound levels higher than 70 dB SPL.

Confocal image analysis

The confocal image dataset consisted of 32 slides of the MNTB from 7 young gerbils and 26 slides from 5 old gerbils (Poleg et al., 2024). The number of MNTB cells was automatically counted with a customized script using the scikit-image library. Each 2D section of the z-stack was binarized using the Otsu thresholding algorithm (Otsu, 1979). Next, the binarized images were subtracted by the background obtained by the top-hat transform, and processed with a morphological erosion operation. The number of cells of the image was approximated by counting the number of contours detected in the processed image. The mean cell counts over all z-stacks were computed as the number of MNTB cells of the slide.

Data Accessibility

The implementation source code of the presented model will be available on a public repository after this manuscript is accepted.

Results:

We developed a spiking model of the auditory brainstem. This model was tested for accuracy against both mouse and gerbil data. We also tested the model's ability to predict changes in the ABR waveforms in two conditions: Fragile x syndrome in *Fmr1*-KO mice and age-related changes to the ABR in gerbils. This allowed us to challenge the model but also importantly to study t the underlying neural changes in aging and autism.

Modeling of ABRs in Fragile x syndrome

Alterations to ABRs have been reported both in children and adults with autism spectrum disorder, including prolonged ABR latencies (Miron et al., 2016) and altered peak amplitudes (Santos et al., 2017; ElMoazen et al., 2020). To further investigate the neural mechanisms in the auditory pathway that might be present in autism, we used the model to simulate the ABRs in *Fmr1*-KO mice. Fragile X syndrome is the most common monogenetic form of autism spectrum disorder and it commonly causes auditory processing deficits in the auditory brain stem, as well as neurodivergent development (Arnett et al., 2014; McCullagh et al., 2017, 2020). Starting with the existing wild type model, we developed the *Fmr1*-KO model by tuning the parameters to match previous reports in Fragile X syndrome, including hyperexcitability (Garcia-Pino et al., 2017) and myelination deficits (Lucas et al., 2021). This was done by enhancing excitatory connectivity and slowing down axonal conduction velocity, respectively. Specifically, the *Fmr1*-KO model included doubled connectivity ($p_{connect}$) in the SBC-to-LSO pathway from 4% to 8% (Garcia-Pino et al., 2017), and increased transmission delay ($\bar{t}_{trans}$) from the GBC to the MNTB by 0.2 ms based on the decreased conduction velocity calculated from the change in the myelin thickness in *Fmr1*-KO mice (Lucas et al., 2021) using a previously published propagation model for myelinated axons (Ford et al., 2015; Arancibia-Cárcamo et al., 2017).

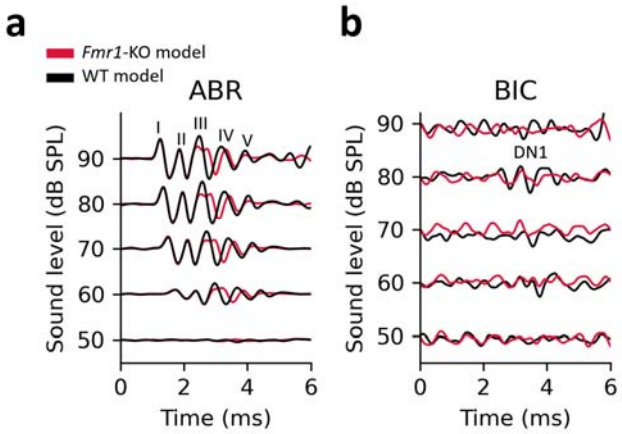

Figure 4. Modeled click ABRs (a) and BICs (b) in the *Fmr1*-KO (red) vs. wild type control (black) models over different sound levels. (band-pass filtered)

Figure 4 shows click ABR and BIC responses over a range of sound intensity levels. Wave III was delayed and attenuated in the *Fmr1*-KO model and the waves IV-V were delayed when compared to the wild-type simulation (Fig.4a). Therefore, previously reported myelination deficits and hyperexcitability in the *Fmr1*-KO can alter ABR morphology. In addition, the BIC DN1 peak of *Fmr1*-KO mice was reduced (Fig.4b), delayed, or absent. Reduced BIC amplitude is associated with behavioral deficits in binaural and spatial hearing tasks in human (Laumen et al., 2016a) and animal models (Anbuhl et al., 2024) of various hearing pathologies. Thus, the finding of reduced amplitude BIC here suggests a compromised sound localization ability in Fragile X syndrome. These results are also consistent with experimental findings suggesting that that *Fmr1*-KO mice showed decreased spatial hearing in behavioral tasks (McCullagh et al., 2020).

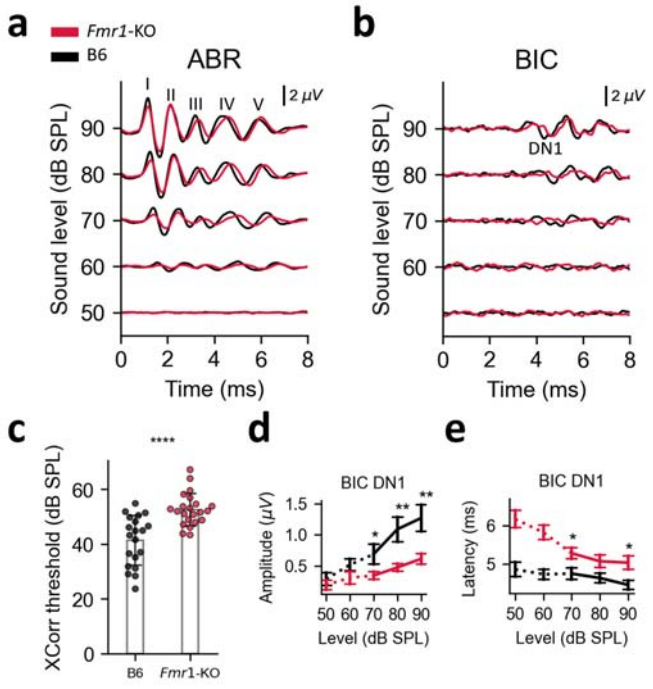

Figure 5. Experimentally recorded ABRs from Fmr1-KO mice (red) and C57BL/6 wildtype controls (black). (a-b) Sample ABR (a) and BIC (b) traces from wildtype and Fmr1-KO mice over different sound intensity levels. (c) Click ABR thresholds estimated with the signal cross-correlation method (Fmr1-KO: 52.61± 5.79 dB SPL (mean ± S.D.); C57BL/6: 41.32 ± 8.89 dB SPL; $p < 0.0001$ in Mann-Whitney U test; error bars: standard deviation). (d-e) BIC-DN1 peak amplitudes (d) and peak latencies (e) of Fmr1-KO vs. C57BL/6 mice (*: $p<0.05$; **: $p<0.01$; Mann-Whitney U test; error bars: standard error of the mean).

To verify the predictions raised by the computational ABRs, click ABR recordings were performed on Fmr1-KO and C57BL/6 wildtype mice (Fig.5). The experimentally recorded ABR traces (Fig.5a) closely matched the simulated ABRs (Fig.4a). Specifically, wave III was attenuated, and waves III-V were delayed in the Fmr1-KO condition. In addition, ABR thresholds were significantly raised by ~10 dB SPL in the *Fmr1*-KO mice (Fig.5c) (*Fmr1*-KO: 52.61± 5.79 dB SPL (mean ± S.D.); C57BL/6: 41.32 ± 8.89 dB SPL; $p < 0.0001$ in Mann-Whitey U test). and BICs were significantly attenuated and delayed (Fig.5d,e).

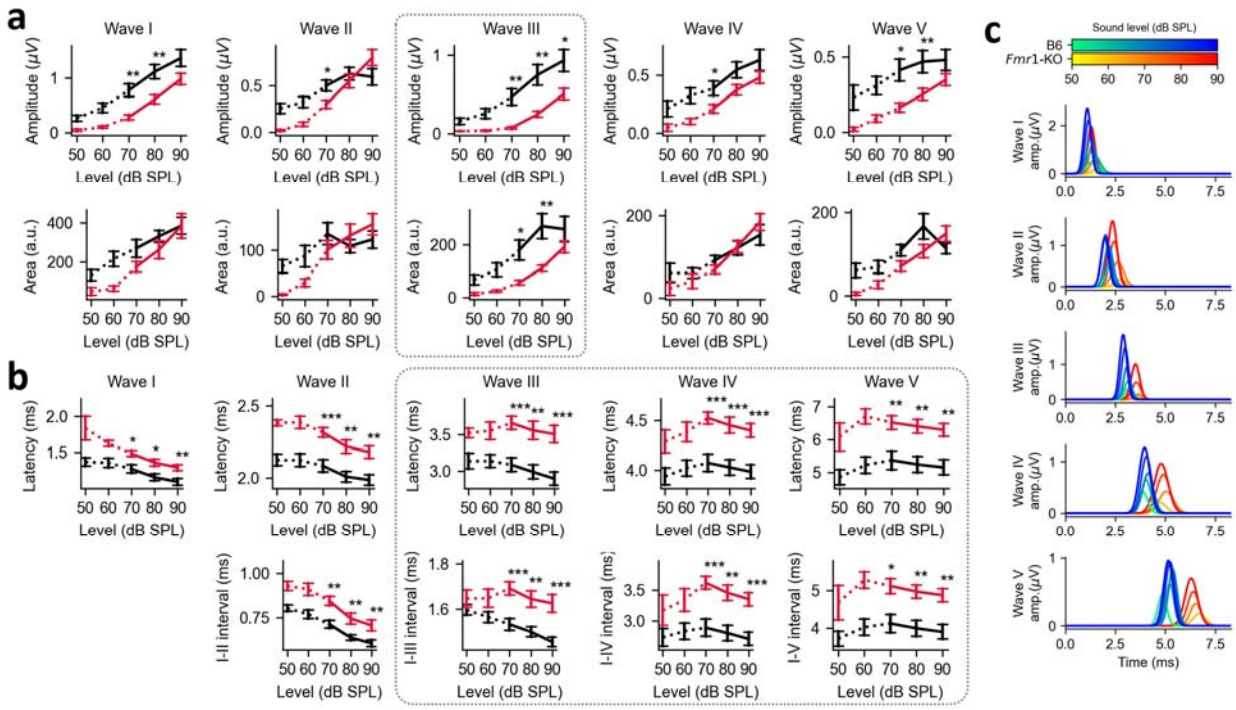

Figure 6. Peak metrics of experimentally measured ABR traces from *Fmr1*-KO mice vs. C57BL/6 wild type controls. (a) Peak amplitudes (top) and surface areas (bottoms). (b) Peak latencies (top) and intervals relative to wave I (bottom). (c) Overall ABR waves based on the average peak metrics from Fmr1-KO mice (orange lines) and C57BL/6 mice (blue lines). (*: $p<0.05$; **: $p<0.01$; ***: $p<0.001$; Mann-Whitney U test; error bar: standard error of the mean)

The statistics and reconstructed visualizations of the Fmr1-KO vs. wild type mouse ABRs are displayed in Fig.6. Despite the raised ABR threshold, the largest change was observed in wave III, which was significantly attenuated in Fmr1-KO mice (Fig.6a). Additionally, longer latencies were observed for wave III-V in KO mice (Fig.6b). The reconstructed ABR waves (Fig.6c) were calculated by fitting Gaussian functions with the averaged peak metrics. These reconstructions also show a significantly reduced wave III, and a longer latency for the following waves. These experimental results suggest that our model successfully predicts the alterations of ABR morphologies in Fragile X syndrome. Moreover, the experimentally reported myelin deficits and hyperexcitability in Fmr1-KO mice are sufficient to

recapitulate the distorted ABR morphology in our model. Behaviorally, these alterations are consistent with the previously reported degradation of binaural and sound localization abilities.

Modeling aging-related alterations in auditory brainstem

Our previous experimental study reported changes in ABR morphology in old gerbils (N=30; ages between P750 to P1167) along with alterations in myelination in the GBC-MNTB pathway and a reduction of mature oligodendrocytes in the trapezoid body when compared to young animals (N = 62; ages between P60 to P109) (Poleg et al., 2024). Briefly, in this dataset, wave I, wave III and wave IV were significantly attenuated, and the latency of wave IV was significantly shorter in old gerbils (Fig.7). As in the Fragile X model, the strongest difference was observed in wave III was the most substantially degraded wave (Fig.7e). Notably, the presence and amplitude of wave III correlates with the integrity of the MNTB or its output (Wada and Starr, 1983, 1989; Jalabi et al., 2013), suggesting altered MNTB activities in both aging and autistic animal models. These gerbil data are consistent with human studies (Konrad-Martin et al., 2012), which also report a wave III decrease in older subjects. Moreover, the BIC-DN1 was decreased and had a shorter latency in old gerbils (Fig.7b). Thresholds of click ABRs did not significantly depend on age (Fig.7d; Young: 32.01 ± 12.71 dB SPL (mean ± SD); old: 29.86 ± 12.00 dB SPL; P = 0.4841, Mann Whiteney U test).

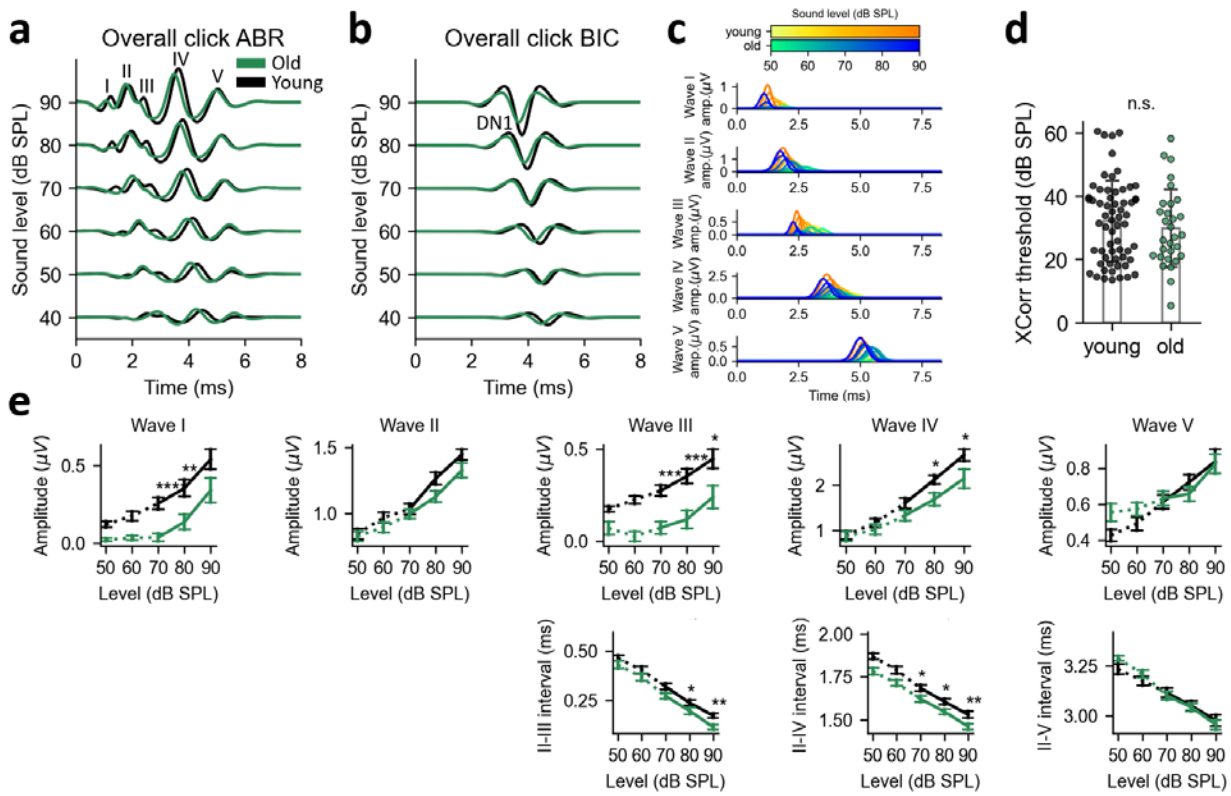

Figure 7. Experimentally recorded click ABRs and analysis of peak metrics in old (green) and young (black) gerbils. This is the same dataset as reported in (Poleg et al., 2024). (a-c) Overall click ABRs (a), BICs (b), and ABR waves (c) reconstructed using averaged peak metrics quantified from all experimentally recorded ABR traces. (d) Click ABR thresholds of old and young gerbils approximated with the signal cross-correlation (Young: 32.01 ± 12.71 dB SPL (mean ± SD); old: 29.86 ± 12.00 dB SPL; P = 0.4841, Mann Whiteney U test; error bar: standard deviation). (e) Peak amplitudes of ABR waves and the relative intervals from wave II. (*: p<0.05; **: p<0.01; ***: p<0.001; Mann-Whitney U test; error bars: standard error of the mean)

Based on these findings, an ABR model of aging gerbils was developed to study the causal relationship between the reported age-related changes in auditory brainstem and the altered ABR waves. Similarly to the development of the Fragile X model, several neuronal parameters were adjusted to establish this aging model. Again, the experimentally observed altered myelination leads to an increase in the modeled transmission delay ( ) from the GBC to the MNTB by 0.2 ms (Poleg et al., 2024). The excitatory

postsynaptic conductance ( ) of the Calyx of Held was decreased from 100 nS to 50 nS due to maller MNTB soma size in old gerbils (Gleich and Strutz, 2002), as well as the smaller coverage ratio of the calyx of held in old rat (Casey and Feldman, 1988). Additionally, the number of MNTB cells was reduced from 1000 per side to 700 per side in the aging model. As all these modifications did not affect signaling at the level of cochlear nuclei, the aging model could diverge from control only in waves III-IV.

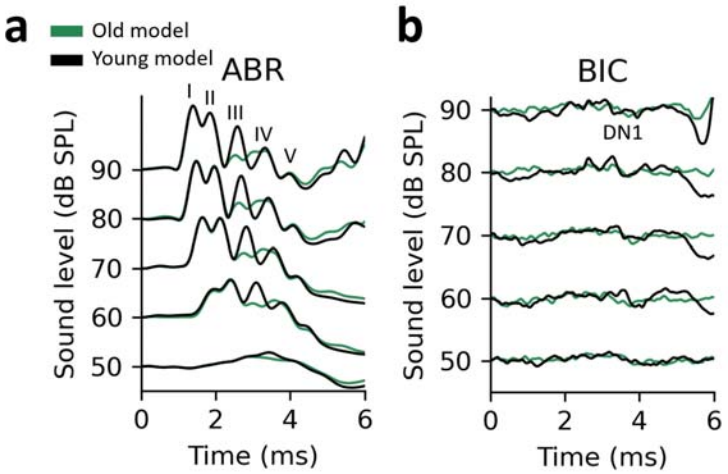

Figure 8. Simulated click ABRs (a) and BICs (b) in aging (green) and young (black) models over different sound levels (unfiltered raw traces).

Simulated ABRs and BICs in the aging model present a trend with smaller or absent wave III and earlier onset of wave IV, consistent with the experimentally recorded ABR changes in old gerbils. Therefore, the altered ABR wave III and wave IV in old gerbils could be explained by the demyelination and degradation along the contralateral inhibitory pathway in the superior olivary complex.

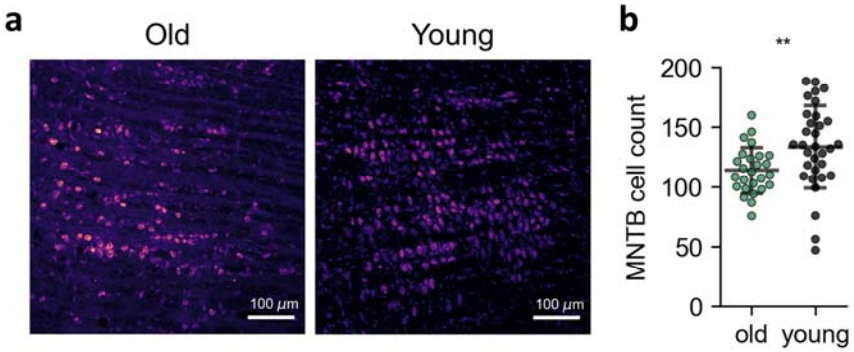

Figure 9. Quantifying MNTB cells in old and young gerbils. (a) Confocal images of MNTB sections from old gerbils (left) and young gerbils (right). (error bar: 100 um) (b) Estimated number of MNTB cells per 640 um * 640 um slide. (Old: 113.49 ± 18.90 cells, N_{animal} = 5, n_{slides} = 26; Young: 133.33 ± 34.51 cells, N_{animal} = 7, n_{slides} = 32; p = 0.0038, Mann-Whiteney U test; error bar: standard deviation)

This particular aging model contains an assumption that the number of MNTB cells is reduced in aged gerbils. Although a reduction in the MNTB cell count was reported in old C57BL/6 mice (Chequer Charan et al., 2022), this strain exhibits severe hearing loss as early as 6 months, and this phenomenon may not occur in other strains and species (Keithley et al., 2004; Fujita et al., 2015). To further explore this point, MNTB cell counts were performed from confocal images in old gerbils. In these confocal images, MNTB neurons were sparser in old gerbils than in young animals (Fig.9a). The estimated cell counts were significantly different with relatively fewer cells in sections from old gerbils (Fig.9b; Old: 113.49 ± 18.90 cells, N_{animal} = 5, n_{slides} = 26; Young: 133.33 ± 34.51 cells, N_{animal} = 7, n_{slides} = 32; p = 0.0038, Mann-Whiteney U test). These cell counts further confirm the age-dependent degradation of the contralaterally evoked inhibition by MNTB in old gerbils, exactly as postulated by the computational model.

Discussion:

There are several results of this study: First, we were able to extend an integrate and fire model to a population level such that we could predict ABRs correctly by modeling the neuronal populations of auditory brain stem nuclei involved in the sound localization process. While ABR models have been proposed before, these did either only model single waves of the ABR trace, or lacked the single-cell approach we used here. The model's ability to simulate the ABR trace from wave I to wave V based on neuronal activities provides a considerable advancement in understanding auditory processing and its associated dysfunctions.

Second, our model not only predicted ABRs of the healthy auditory system correctly, but also correctly captured neurological alterations which are present in two conditions, namely autism and age-related central hearing loss. Both of these conditions have in common that affected listeners have trouble isolating a sound source of interest among competing background noises. In such environments, commonly termed “cocktail-party situations”, listeners use their sound localization circuit to spatially segregate sound sources of interest from background sounds based on spatial location. Human listeners with normal hearing are able to localize to 5 spatial degrees or better, such that competing sounds would fall into separate spatial channels as long as they are at least 5 degrees removed from each other. Any alterations in the sound localization pathway which results in less precise spatial location should then lead to difficulties functioning in cocktail party environments. Both listeners with autism spectrum disorder and aging listeners are well known to have difficulties in acoustically busy environments, and in both conditions distinct alterations in the sound localization pathway have been demonstrated across species. These alterations were recapitulated by our model based on reductions in the amplitude of the BIC of the ABR.

Third, the results of this study underscore the utility of computational models in bridging the gap between experimental and computational work. In this particular study, the model predicted a decrease in the number of MNTB principal neurons in aging, which prompted a follow up experimental study with the

goal to test whether this modeling prediction could be verified in anatomical analysis – the prediction was indeed verified. In our opinion, an ideal modeling approach should be both strongly based on experimental data, but should also able to point out potential gaps in the experimental data, and suggest distinct and precise follow up bench experiments, as it happened in this case.

Specifically, the application of the model in Fragile X syndrome recapitulated alterations of the ABR morphology driven by myelin deficits and hyperexcitability, such as decreased wave III amplitudes and prolonged wave III-V intervals. These findings align with previously reported results in children with autism (Rosenhall et al., 2003; Magliaro et al., 2010; O'Connor, 2012). The validation of these simulated results with experimentally recorded ABRs from Fmr1-KO mice suggests that the myelin deficits and hyperexcitability are sufficient to cause the observed ABR alterations and are also consistent with auditory phenotypes in autism. These findings support potential therapeutical approaches through remyelination (Shen et al., 2018) or by modulating neuronal connectivity (Srivastava and Penzes, 2011).

Regarding the aging phenotype, our model successfully approximated the ABRs recorded from aging gerbils, revealing deficits in the contralateral inhibitory pathway and a decrease in the cell count in MNTB, which was subsequently validated in confocal images. These results confirm a prior study showing reduced wave I, III, IV and BIC in aged gerbils (Laumen et al., 2016b). Again, these findings suggest therapeutic approaches in restoring this form of age-related hearing loss in elderly individuals through remyelination (Gingele et al., 2020) and by enhancing contralateral inhibition. We note that while contralateral inhibition has been investigated in many studies, the ipsilateral inhibition via LNTB is much less understood, and we do not know if this projection also altered in autism or aging. Because of the paucity of experimental data, we were unable to assess potential roles of this projection in Fragile X or aging in the model.

The results presented here were obtained by using relatively simple spiking neuron models with homogeneous configurations. Future work could focus on integrating more detailed neural models with heterogenous cell types, or involve complex sound stimuli, for example binaural cues (Ferber et al., 2016)

or speech (Skoe and Kraus, 2010). This would enhance the model's accuracy in simulating complex auditory processing tasks and disorders. Additionally, the model's application could be extended to other neurological conditions that affect auditory processing and brain stem functions, such as schizophrenia (Juselius Baghdassarian et al., 2018), multiple sclerosis (Japaridze et al., 2002), or brain injury (Benghanem et al., 2020).

In summary, the proposed computational model of the auditory brainstem developed in this study serves as a useful tool for linking ABR recordings to the underlying neural mechanisms. The validation of the model in both autistic and aging animal models suggests its potential for various applications in auditory research and diagnostics. Future advancements in this modeling approach may provide further insights into the complexities of auditory processing.

References:

Anbuhl KL, Ferber AT, Brown AD, Benichoux V, Greene NT, Tollin DJ (2024) Unilateral auditory deprivation reveals brainstem origin of a sensitive period for spatial hearing. Available at: http://biorxiv.org/lookup/doi/10.1101/2024.04.01.587638 [Accessed August 4, 2024].

Arancibia-Cárcamo IL, Ford MC, Cossell L, Ishida K, Tohyama K, Attwell D (2017) Node of Ranvier length as a potential regulator of myelinated axon conduction speed. eLife 6:e23329.

Arnett MT, Herman DH, McGee AW (2014) Deficits in Tactile Learning in a Mouse Model of Fragile X Syndrome Bardoni B, ed. PLoS ONE 9:e109116.

Ashida G, Kretzberg J, Tollin DJ (2016) Roles for Coincidence Detection in Coding Amplitude-Modulated Sounds Chase SM, ed. PLoS Comput Biol 12:e1004997.

Beiderbeck B, Myoga MH, Müller NIC, Callan AR, Friauf E, Grothe B, Pecka M (2018) Precisely timed inhibition facilitates action potential firing for spatial coding in the auditory brainstem. Nat Commun 9:1771.

Benghanem S, Mazeraud A, Azabou E, Chhor V, Shinotsuka CR, Claassen J, Rohaut B, Sharshar T (2020) Brainstem dysfunction in critically ill patients. Crit Care 24:5.

Benichoux V, Ferber A, Hunt S, Hughes E, Tollin D (2018) Across Species “Natural Ablation” Reveals the Brainstem Source of a Noninvasive Biomarker of Binaural Hearing. J Neurosci 38:8563–8573.

Brand A, Behrend O, Marquardt T, McAlpine D, Grothe B (2002) Precise inhibition is essential for microsecond interaural time difference coding. Nature 417:543–547.

Casey MA, Feldman ML (1988) Age-related loss of synaptic terminals in the rat medial nucleus of the trapezoid body. Neuroscience 24:189–194.

Chequer Charan D, Hua Y, Wang H, Huang W, Wang F, Elgoyhen AB, Boergens KM, Di Guilmi MN (2022) Volume electron microscopy reveals age-related circuit remodeling in the auditory brainstem. Front Cell Neurosci 16:1070438.

Chon U, Vanselow DJ, Cheng KC, Kim Y (2019) Enhanced and unified anatomical labeling for a common mouse brain atlas. Nat Commun 10:5067.

Couchman K, Grothe B, Felmy F (2010) Medial Superior Olivary Neurons Receive Surprisingly Few Excitatory and Inhibitory Inputs with Balanced Strength and Short-Term Dynamics. J Neurosci 30:17111–17121.

ElMoazen D, Sobhy O, Abdou R, AbdelMotaleb H (2020) Binaural interaction component of the auditory brainstem response in children with autism spectrum disorder. International Journal of Pediatric Otorhinolaryngology 131:109850.

Encke J, Hemmert W (2018) Extraction of Inter-Aural Time Differences Using a Spiking Neuron Network Model of the Medial Superior Olive. Front Neurosci 12:140.

Fan L, Li H, Zhuo J, Zhang Y, Wang J, Chen L, Yang Z, Chu C, Xie S, Laird AR, Fox PT, Eickhoff SB, Yu C, Jiang T (2016) The Human Brainnetome Atlas: A New Brain Atlas Based on Connectional Architecture. Cereb Cortex 26:3508–3526.

Ferber AT, Benichoux V, Tollin DJ (2016) Test-Retest Reliability of the Binaural Interaction Component of the Auditory Brainstem Response. Ear & Hearing 37:e291–e301.

Ford MC, Alexandrova O, Cossell L, Stange-Marten A, Sinclair J, Kopp-Scheinpflug C, Pecka M, Attwell D, Grothe B (2015) Tuning of Ranvier node and internode properties in myelinated axons to adjust action potential timing. Nat Commun 6:8073.

Fujita T, Yamashita D, Uehara N, Inokuchi G, Hasegawa S, Otsuki N, Nibu K (2015) A High-Fat Diet Delays Age-Related Hearing Loss Progression in C57BL/6J Mice Smith B, ed. PLoS ONE 10:e0117547.

Garcia-Pino E, Gessele N, Koch U (2017) Enhanced Excitatory Connectivity and Disturbed Sound Processing in the Auditory Brainstem of Fragile X Mice. J Neurosci 37:7403–7419.

Gingele S, Henkel F, Heckers S, Moellenkamp TM, Hümmert MW, Skripuletz T, Stangel M, Gudi V (2020) Delayed Demyelination and Impaired Remyelination in Aged Mice in the Cuprizone Model. Cells 9:945.

Gleich O, Strutz J (2002) Age dependent changes in the medial nucleus of the trapezoid body in gerbils. Hearing Research 164:166–178.

Grothe B, Pecka M, McAlpine D (2010) Mechanisms of Sound Localization in Mammals. Physiological Reviews 90:983–1012.

Hernandez VH, Gehrt A, Reuter K, Jing Z, Jeschke M, Mendoza Schulz A, Hoch G, Bartels M, Vogt G, Garnham CW, Yawo H, Fukazawa Y, Augustine GJ, Bamberg E, Kügler S, Salditt T, De Hoz L, Strenzke N, Moser T (2014) Optogenetic stimulation of the auditory pathway. J Clin Invest 124:1114–1129.

Hodgkin AL, Huxley AF (1952) A quantitative description of membrane current and its application to conduction and excitation in nerve. The Journal of Physiology 117:500–544.

Izhikevich EM (2003) Simple model of spiking neurons. IEEE Trans Neural Netw 14:1569–1572.

Jalabi W, Kopp-Scheinpflug C, Allen PD, Schiavon E, DiGiacomo RR, Forsythe ID, Maricich SM (2013) Sound Localization Ability and Glycinergic Innervation of the Superior Olivary Complex Persist after Genetic Deletion of the Medial Nucleus of the Trapezoid Body. J Neurosci 33:15044–15049.

Japaridze G, Shakarishvili R, Kevanishvili Z (2002) Auditory brainstem, middle-latency, and slow cortical responses in multiple sclerosis: ABRs, MLRs, and SCPs in MS. Acta Neurologica Scandinavica 106:47–53.

Johnson KL, Nicol TG, Kraus N (2005) Brain Stem Response to Speech: A Biological Marker of Auditory Processing. Ear & Hearing 26:424–434.

Juselius Baghdassarian E, Nilsson Markhed M, Lindström E, Nilsson BM, Lewander T (2018) Auditory brainstem response (ABR) profiling tests as diagnostic support for schizophrenia and adult attention-deficit hyperactivity disorder (ADHD). Acta Neuropsychiatr 30:137–147.

Keithley EM, Canto C, Zheng QY, Fischel-Ghodsian N, Johnson KR (2004) Age-related hearing loss and the ahl locus in mice. Hearing Research 188:21–28.

Keplinger S, Beiderbeck B, Michalakis S, Biel M, Grothe B, Kunz L (2018) Optogenetic Control of Neural Circuits in the Mongolian Gerbil. Front Cell Neurosci 12:111.

Konrad-Martin D, Dille MF, McMillan G, Griest S, McDermott D, Fausti SA, Austin DF (2012) Age-Related Changes in the Auditory Brainstem Response. J Am Acad Audiol 23:018–035.

Laumen G, Ferber AT, Klump GM, Tollin DJ (2016a) The Physiological Basis and Clinical Use of the Binaural Interaction Component of the Auditory Brainstem Response. Ear & Hearing 37:e276–e290.

Laumen G, Tollin DJ, Beutelmann R, Klump GM (2016b) Aging effects on the binaural interaction component of the auditory brainstem response in the Mongolian gerbil: Effects of interaural time and level differences. Hearing Research 337:46–58.

Li B-Z, Pun SH, Vai MI, Lei TC, Klug A (2022) Predicting the Influence of Axon Myelination on Sound Localization Precision Using a Spiking Neural Network Model of Auditory Brainstem. Front Neurosci 16:840983.

Liberman MC (1978) Auditory-nerve response from cats raised in a low-noise chamber. The Journal of the Acoustical Society of America 63:442–455.

Lucas A, Poleg S, Klug A, McCullagh EA (2021) Myelination Deficits in the Auditory Brainstem of a Mouse Model of Fragile X Syndrome. Front Neurosci 15:772943.

Magliaro FCL, Scheuer CI, Assumpção Júnior FB, Matas CG (2010) Estudo dos potenciais evocados auditivos em autismo. Pró-Fono R Atual Cient 22:31–36.

McCullagh EA, Poleg S, Greene NT, Huntsman MM, Tollin DJ, Klug A (2020) Characterization of Auditory and Binaural Spatial Hearing in a Fragile X Syndrome Mouse Model. eNeuro 7:ENEURO.0300-19.2019.

McCullagh EA, Salcedo E, Huntsman MM, Klug A (2017) Tonotopic alterations in inhibitory input to the medial nucleus of the trapezoid body in a mouse model of Fragile X syndrome. J of Comparative Neurology 525:3543–3562.

Melcher JR, Kiang NYS (1996) Generators of the brainstem auditory evoked potential in cat III: identified cell populations. Hearing Research 93:52–71.

Miron O, Ari‐Even Roth D, Gabis LV, Henkin Y, Shefer S, Dinstein I, Geva R (2016) Prolonged auditory brainstem responses in infants with autism. Autism Research 9:689–695.

Møller AR, Jannetta PJ (1985) Neural generators of the auditory brainstem response. In: The auditory brainstem response, pp 13–31.

O'Connor K (2012) Auditory processing in autism spectrum disorder: A review. Neuroscience & Biobehavioral Reviews 36:836–854.

Oertel D, Cao X-J, Ison JR, Allen PD (2017) Cellular Computations Underlying Detection of Gaps in Sounds and Lateralizing Sound Sources. Trends in Neurosciences 40:613–624.

Otsu N (1979) A Threshold Selection Method from Gray-Level Histograms. IEEE Trans Syst, Man, Cybern 9:62–66.

Poleg S, Li B-Z, Ridenour M, Hughes EG, Tollin D, Klug A (2024) Age-related myelin deficits in the auditory brain stem contribute to cocktail party-deficits. bioRxiv:2024.07.29.605710.

Radtke-Schuller S, Schuller G, Angenstein F, Grosser OS, Goldschmidt J, Budinger E (2016) Brain atlas of the Mongolian gerbil (Meriones unguiculatus) in CT/MRI-aided stereotaxic coordinates. Brain Struct Funct 221:1–272.

Rattay F, Danner SM (2014) Peak I of the human auditory brainstem response results from the somatic regions of type I spiral ganglion cells: Evidence from computer modeling. Hearing Research 315:67–79.

Roberts MT, Seeman SC, Golding NL (2014) The relative contributions of MNTB and LNTB neurons to inhibition in the medial superior olive assessed through single and paired recordings. Front Neural Circuits 8 Available at: http://journal.frontiersin.org/article/10.3389/fncir.2014.00049/abstract [Accessed May 23, 2023].

Rosenhall U, Nordin V, Brantberg K, Gillberg C (2003) Autism and Auditory Brain Stem Responses: Ear and Hearing 24:206–214.

Rudnicki M, Schoppe O, Isik M, Völk F, Hemmert W (2015) Modeling auditory coding: from sound to spikes. Cell Tissue Res 361:159–175.

Saiz-Alía M, Reichenbach T (2020) Computational modeling of the auditory brainstem response to continuous speech. J Neural Eng 17:036035.

Santos M, Marques C, Nóbrega Pinto A, Fernandes R, Coutinho MB, Almeida E Sousa C (2017) Autism spectrum disorders and the amplitude of auditory brainstem response wave I: Autism spectrum disorders and the amplitude of ABR wave I. Autism Research 10:1300–1305.

Shen H-Y, Huang N, Reemmer J, Xiao L (2018) Adenosine Actions on Oligodendroglia and Myelination in Autism Spectrum Disorder. Front Cell Neurosci 12:482.

Skoe E, Kraus N (2010) Auditory Brain Stem Response to Complex Sounds: A Tutorial. Ear & Hearing 31:302–324.

Spirou GA, Rager J, Manis PB (2005) Convergence of auditory-nerve fiber projections onto globular bushy cells. Neuroscience 136:843–863.

Srivastava DP, Penzes P (2011) Rapid Estradiol Modulation of Neuronal Connectivity and Its Implications for Disease. Front Endocrin 2 Available at: http://journal.frontiersin.org/article/10.3389/fendo.2011.00077/abstract [Accessed July 30, 2024].

Stimberg M, Brette R, Goodman DF (2019) Brian 2, an intuitive and efficient neural simulator. eLife 8:e47314.

Suthakar K, Liberman MC (2019) A simple algorithm for objective threshold determination of auditory brainstem responses. Hearing Research 381:107782.

Verhulst S, Altoè A, Vasilkov V (2018) Computational modeling of the human auditory periphery: Auditory-nerve responses, evoked potentials and hearing loss. Hearing Research 360:55–75.

Verhulst S, Bharadwaj HM, Mehraei G, Shera CA, Shinn-Cunningham BG (2015) Functional modeling of the human auditory brainstem response to broadband stimulation. The Journal of the Acoustical Society of America 138:1637–1659.

Wada S-I, Starr A (1983) Generation of auditory brain stem responses (ABRs). III. Effects of lesions of the superior olive, lateral lemniscus and inferior colliculus on the ABR in guinea pig. Electroencephalography and Clinical Neurophysiology 56:352–366.

Wada S-I, Starr A (1989) Anatomical bases of binaural interaction in auditory brain-stem responses from guinea pig. Electroencephalography and Clinical Neurophysiology 72:535–544.

Zilany MSA, Bruce IC, Carney LH (2014) Updated parameters and expanded simulation options for a model of the auditory periphery. The Journal of the Acoustical Society of America 135:283–286.

Figure Legends:

Figure 1. Schematic of the ABR recording setup (top) and sources of ABR waves (bottom).

Figure 2. Network architecture of the auditory brainstem model.

Figure 3. Workflow of modeling ABRs. (a) The auditory brain stem that was modeled. (b) Peri-stimulus time histograms induced by encoding click sounds averaged across all neurons for each nucleus. (c) Approximated field potentials from histograms. (d) Exponentially attenuated amplitudes and linearly increased latencies for field potentials propagating over distance. (e) Final ABRs modeled by propagating and integrating field potentials according to the geometric distribution of the nuclei and electrode location.

Figure 4. Modeled click ABRs (a) and BICs (b) in the *Fmr1*-KO (red) vs. wild type control (black) models over different sound levels. (band-pass filtered)

Figure 5. Experimentally recorded ABRs from Fmr1-KO mice (red) and C57BL/6 wildtype controls (black). (a-b) Sample ABR (a) and BIC (b) traces from wildtype and Fmr1-KO mice over different sound intensity levels. (c) Click ABR thresholds estimated with the signal cross-correlation method (Fmr1-KO: 52.61± 5.79 dB SPL (mean ± S.D.); C57BL/6: 41.32 ± 8.89 dB SPL; $p < 0.0001$ in Mann-Whitney U test; error bars: standard deviation). (d-e) BIC-DN1 peak amplitudes (d) and peak latencies (e) of Fmr1-KO vs. C57BL/6 mice (*: $p<0.05$; **: $p<0.01$; Mann-Whitney U test; error bars: standard error of the mean).

Figure 6. Peak metrics of experimentally measured ABR traces from *Fmr1*-KO mice vs. C57BL/6 wild type controls. (a) Peak amplitudes (top) and surface areas (bottoms). (b) Peak latencies (top) and intervals relative to wave I (bottom). (c) Overall ABR waves based on the average peak metrics from Fmr1-KO mice (orange lines) and C57BL/6 mice (blue lines). (*: $p<0.05$; **: $p<0.01$; ***: $p<0.001$; Mann-Whitney U test; error bar: standard error of the mean)

Figure 7. Experimentally recorded click ABRs and analysis of peak metrics in old (green) and young (black) gerbils. This is the same dataset as reported in (Poleg et al., 2024). (a-c) Overall click ABRs (a),

BICs (b), and ABR waves (c) reconstructed using averaged peak metrics quantified from all experimentally recorded ABR traces. (d) Click ABR thresholds of old and young gerbils approximated with the signal cross-correlation (Young: 32.01 ± 12.71 dB SPL (mean ± SD); old: 29.86 ± 12.00 dB SPL; P = 0.4841, Mann Whiteney U test; error bar: standard deviation). (e) Peak amplitudes of ABR waves and the relative intervals from wave II. (*: $p<0.05$; **: $p<0.01$; ***: $p<0.001$; Mann-Whitney U test; error bars: standard error of the mean)

Figure 8. Simulated click ABRs (a) and BICs (b) in aging (green) and young (black) models over different sound levels.

Figure 9. Quantifying MNTB cells in old and young gerbils. (a) Confocal images of MNTB sections from old gerbils (left) and young gerbils (right). (error bar: 100 um) (b) Estimated number of MNTB cells per 640 um * 640 um slide. (Old: 113.49 ± 18.90 cells, $N_{animal} = 5$, $n_{slides} = 26$; Young: 133.33 ± 34.51 cells, $N_{animal} = 7$, $n_{slides} = 32$; p = 0.0038, Mann-Whiteney U test; error bar: standard deviation)

Table Legends:

Table 1. List of parameters for neurons and synapses

Table 2. List of network parameters for the auditory brainstem model